This is a repository copy of *IRIS Burst Spectra Co-Spatial To A Quiet-Sun Ellerman-Like Brightening*.

White Rose Research Online URL for this paper:
http://eprints.whiterose.ac.uk/119321/

Version: Published Version

Article:
Nelson, C.J., Freij, N., Reid, A. et al. (3 more authors) (2017) IRIS Burst Spectra Co-Spatial To A Quiet-Sun Ellerman-Like Brightening. The Astrophysical Journal, 845 (1). 16. ISSN 0004-637X

https://doi.org/10.3847/1538-4357/aa7e7a

Reuse
This article is distributed under the terms of the Creative Commons Attribution (CC BY) licence. This licence allows you to distribute, remix, tweak, and build upon the work, even commercially, as long as you credit the authors for the original work. More information and the full terms of the licence here: https://creativecommons.org/licenses/

Takedown
If you consider content in White Rose Research Online to be in breach of UK law, please notify us by emailing eprints@whiterose.ac.uk including the URL of the record and the reason for the withdrawal request.

eprints@whiterose.ac.uk
https://eprints.whiterose.ac.uk/

The Astrophysical Journal, 845:16 (11pp), 2017 August 10 https://doi.org/10.3847/1538-4357/aa7e7a
© 2017. The American Astronomical Society. All rights reserved.
OPEN ACCESS

IRIS Burst Spectra Co-spatial to a Quiet-Sun Ellerman-like Brightening

C. J. Nelson[1,2], N. Freij[3], A. Reid[2], R. Oliver[3,4], M. Mathioudakis[2], and R. Erdélyi[1,5]
[1] Solar Physics and Space Plasma Research Centre, University of Sheffield, Hicks Building, Hounsfield Road, Sheffield, S3 7RH, UK; c.j.nelson@sheffield.ac.uk
[2] Astrophysics Research Centre (ARC), School of Mathematics and Physics, Queens University, Belfast, BT7 1NN, UK
[3] Departament de Física, Universitat de les Illes Balears, E-07122 Palma de Mallorca, Spain
[4] Institut d'Aplicacions Computacionals de Codi Comunitari (IAC^3), Universitat de les Illes Balears, E-07122 Palma de Mallorca, Spain
[5] Department of Astronomy, Eötvös Loránd University, Budapest P.O. Box 32, H-1518, Hungary
Received 2017 May 11; revised 2017 June 23; accepted 2017 July 2; published 2017 August 8

Abstract

Ellerman bombs (EBs) have been widely studied over the past two decades; however, only recently have the counterparts of these events been observed in the quiet-Sun. The aim of this article is to further understand small-scale quiet-Sun Ellerman-like brightenings (QSEBs) through research into their spectral signatures, including investigating whether the hot signatures associated with some EBs are also visible co-spatial to any QSEBs. We combine Hα and Ca II 8542 Å line scans at the solar limb with spectral and imaging data sampled by the *Interface Region Imaging Spectrograph* (*IRIS*). Twenty-one QSEBs were identified with average lifetimes, lengths, and widths measured to be around 120 s, 0.″63, and 0.″35, respectively. Three of these QSEBs displayed clear repetitive flaring through their lifetimes, comparable to the behavior of EBs in active regions. Two QSEBs in this sample occurred co-spatial to increased emission in *SDO*/AIA 1600 Å and *IRIS* slit-jaw imager 1400 Å data; however, these intensity increases were smaller than those reported co-spatially with EBs. One QSEB was also sampled by the *IRIS* slit during its lifetime, displaying increases in intensity in the Si IV 1393 Å and Si IV 1403 Å cores, as well as the C II and Mg II line wings, analogous to *IRIS* bursts (IBs). Using RADYN simulations, we are unable to reproduce the observed QSEB Hα and Ca II 8542 Å line profiles, leaving the question of the temperature stratification of QSEBs open. Our results imply that some QSEBs could be heated to transition region temperatures, suggesting that IB profiles should be observed throughout the quiet-Sun.

Key words: Sun: atmosphere – Sun: chromosphere – Sun: magnetic fields – Sun: photosphere

1. Introduction

Ellerman bombs (hereafter referred to as EBs) are small-scale (lengths often below 1″), short-lived (lifetimes below 10 minutes) events that were originally identified by Ellerman (1917) as regions of intense brightness in the wings of the Hα line profile. These features were named "petit points" by Lyot (1944) and "moustaches" by Severny (1956), before the term "EBs" was coined by McMath et al. (1960). EBs have been widely observed co-spatial to regions of opposite-polarity magnetic field (see, for example, Georgoulis et al. 2002; Pariat et al. 2004; Watanabe et al. 2011; Reid et al. 2015, 2016) and have been interpreted as the signatures of magnetic reconnection in the photosphere (e.g., Watanabe et al. 2008; Archontis & Hood 2009; Yang et al. 2016). Until recently, these events had been exclusively observed within active regions (ARs), however, new research by Rouppe van der Voort et al. (2016) has indicated the presence of EB-like events in the quiet-Sun, named quiet-Sun Ellerman-like brightenings (QSEBs) to distinguish these events from EBs themselves.

One of the most puzzling aspects of EBs is their appearance, or lack there of, in a range of spectral lines. Identified signatures of these events include increased wing emission in the Ca II 8542 Å (Socas-Navarro et al. 2006), He I D3, and He I 10830 Å (Libbrecht et al. 2016) profiles, as well as enhanced emission in the 1600 Å (Qiu et al. 2000) and 1700 Å continua (Vissers et al. 2013, 2015). Both Ellerman (1917) and Rutten et al. (2015), however, identified no signatures of EBs in the Na I or Mg I b2 lines. Semi-empirical modeling of a variety of combinations of these lines originally led to estimates of heating within the local photospheric plasma ranging from ∼400–2000 K (see, e.g., Kitai 1983; Fang et al. 2006; Berlicki & Heinzel 2014; Grubecka et al. 2016). Temperature increases of this order were challenged by results obtained through analysis of *Interface Region Imaging Spectrograph* (*IRIS*; De Pontieu et al. 2014) data that implied significantly more heating is occurring during the lifetimes of EBs (up to 8×10^4 K).

The identification of small-scale brightening events in the *IRIS* Si IV "Transition Region" (TR) lines was accomplished by Peter et al. (2014), who observed "hot explosions" with estimated temperatures of 8×10^4 K. These authors suggested that such *IRIS* bursts (IBs) could be evidence of heating within photospheric EBs, which could not be directly identified in that work, to temperatures an order of magnitude higher than those predicted by previous semi-empirical modeling. It should be noted, however, that such modeling had, until that point, been conducted under the assumption that EBs occurred in relatively cool photospheric and chromospheric conditions and had not therefore attempted to account for the high temperatures of IBs. In an independent analysis, however, Judge (2015) asserted that these *IRIS* features were instead formed in the chromosphere or above. Links between at least a subset of EBs and IBs were established by Vissers et al. (2015), Kim et al. (2015), and Tian et al. (2016), appearing to support the assertion that it is photospheric plasma contained within EBs that reaches TR temperatures. It should be noted, though, that recent work by Rutten (2016), who assumed that the visibility of EBs could be explained by LTE modeling, has suggested that temperatures as

Original content from this work may be used under the terms of the Creative Commons Attribution 3.0 licence. Any further distribution of this work must maintain attribution to the author(s) and the title of the work, journal citation and DOI.

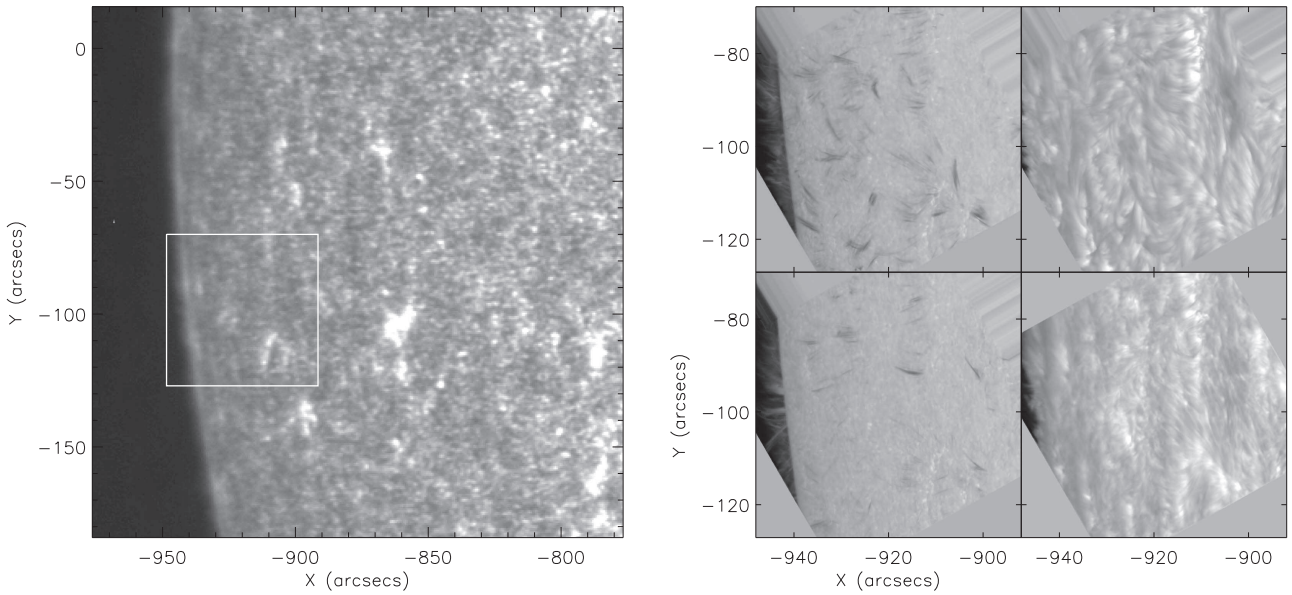

Figure 1. (Left) Context *SDO*/AIA 1700 Å image of the region surrounding the SST/CRISP FOV (white box) sampled at 07:39:17 UT. (Right) Clockwise from the top left are the initial (therefore, temporally closest to the *SDO* frame) SST/CRISP images in the: Hα blue wing (−1 Å), Hα line core, Ca II 8542 Å line core, and Hα red wing (+1 Å).

low as 2×10^4 K could account for the observed increased emission in the Si IV line.

With relation to QSEBs, Rouppe van der Voort et al. (2016) found no evidence of emission signatures in Ca II 8542 Å data, Si IV images (sampled by *IRIS*), or the 1600 and 1700 Å continua, indicating that these events could be formed at lower temperatures or physical heights than their AR cousins. The observed lengths and lifetimes of these events were also smaller than those found for AR EBs in the literature (see, for example, Watanabe et al. 2011; Vissers et al. 2013; Nelson et al. 2015), leading these authors to suggest that QSEBs were a "weaker member" of the small-scale, reconnection-driven family of events in the lower solar atmosphere, possibly consistent with the modeling attempts of Nelson et al. (2013). Notably though, Rouppe van der Voort et al. (2016) only studied slit-jaw images from *IRIS*, and a detailed analysis of the spectra, in order to identify whether typical IB profiles can be observed co-spatial to QSEBs, is still required.

Recently, Reid et al. (2017) used RADYN simulations (Carlsson & Stein 1992, 1995) to model one-dimensional solar atmospheres perturbed by energy deposition at multiple layers. These authors then synthesized Hα and Ca II 8542 Å line profiles, finding that impulsive energy releases in the upper photosphere could account for EB signatures. Whether such techniques and models could reproduce QSEB signatures (i.e., Hα wing emission with no co-temporal Ca II 8542 Å response), however, is still unknown and will be discussed here.

In this article, we aim to further understand both QSEBs and IBs, specifically by researching whether IBs are also evident in the quiet-Sun co-spatial to any QSEBs. We structure our work as follows: in Section 2, we introduce the observations analyzed here. Section 3 presents our results, including the inference of the basic properties of QSEBs and an analysis of the signatures of one of these events in spectra collected by *IRIS*. Finally, we draw our conclusions in Section 4.

2. Observations

The ground-based observations analyzed in this article were acquired with the CRisp Imaging SpectroPolarimeter (CRISP: Scharmer 2006; Scharmer et al. 2008) at the Swedish 1 m Solar Telescope (SST: Scharmer et al. 2003) on 2016 June 9th. A quiet-Sun region (coordinates of $x_c \approx -900''$, $y_c \approx -100''$) was selected for observation between 07:39:29 UT and 08:28:54 UT. The observing sequence applied during this time consisted of a 21-point Hα line scan and a 21-point full-Stokes Ca II 8542 Å line scan, both of which sampled ±2 Å into the wings of the lines. Wide-band images were also acquired for Hα and Ca II 8542 Å at each time-step for alignment purposes. These data were reduced using the multi-object multi-frame blind deconvolution (MOMFBD; van Noort et al. 2005) method, with eight exposures at each wavelength position, and following the CRISPRED pipeline (see de la Cruz Rodríguez et al. 2015). Analysis was conducted, in part, using the CRISPEX package (Vissers & Rouppe van der Voort 2012). The final science-ready cadence and pixel-scale of these data were 26.5 s and 0.″058, respectively.

Co-spatial and co-temporal data from three filters (304, 1600, and 1700 Å) of the *Solar Dynamics Observatory*'s Atmospheric Imaging Assembly (*SDO*/AIA; Lemen et al. 2012) instrument were also analyzed. A $100'' \times 100''$ region centered on the CRISP/SST field of view (FOV) was downloaded for the entire time series. The pixel-scale of these data is approximately 0.″6 (corresponding to around 435 km on the horizontal scale). The cadence of these data is wavelength-dependent: 12 s for the 304 Å data and 24 s for the 1600 and 1700 Å data. Alignment of the *SDO*/AIA filters with the SST/CRISP line scans was achieved by matching the solar limb and stable network bright points within the 1600 Å and wide-band Ca II 8542 Å context images through time. The initial FOV of these data is plotted for reference in Figure 1, which includes a larger *SDO*/AIA 1700 Å context image (left panel) and (clockwise from the top left in the right panel) SST/CRISP images for the Hα blue wing (−1 Å), the Hα line core, the Ca II

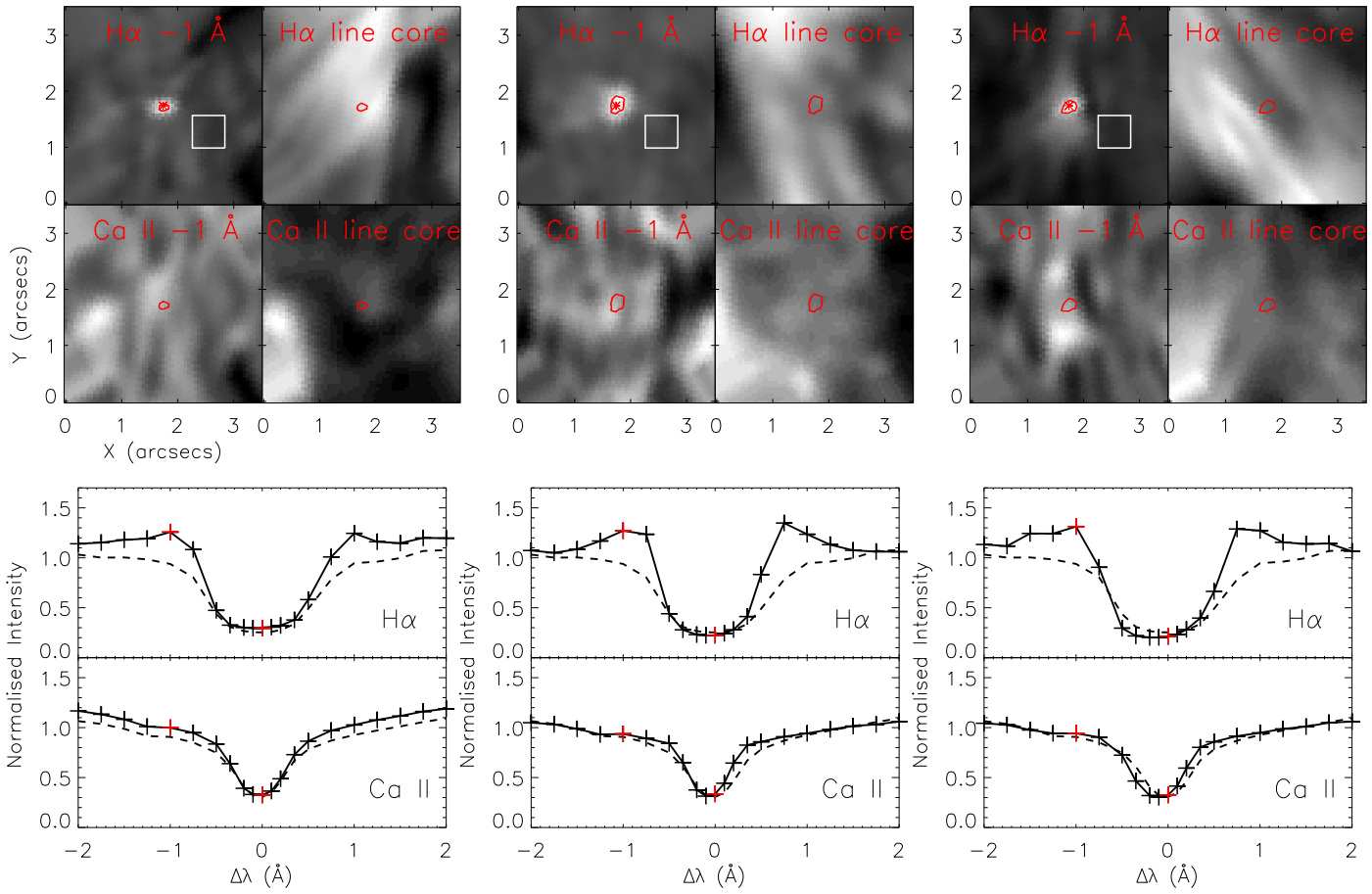

Figure 2. Three representative QSEBs from the sample analyzed here. (Top row) Images collected at various positions within the Hα and Ca II 8542 line profiles (specific line positions are indicated in individual panels). The red cross and white box in the top left panel of each set indicate the pixel and pixels selected to construct the line profiles of the QSEBs and (time-averaged) background atmosphere, respectively. The red contours indicate the pixels over 130% of the background intensity in the Hα line wings. (Bottom row) The Hα and Ca II 8542 Å line profiles measured for the QSEB and the background region. Red crosses indicate the wavelength positions plotted in the top row.

8542 line core, and the Hα red wing (+1 Å). The white box in the left panel indicates the SST/CRISP FOV.

Finally, data from the *IRIS* satellite were also analyzed. *IRIS* collected five dense 320-step rasters between 07:31:21 UT and 11:39:14 UT, with the first raster coinciding temporally with the SST/CRISP observations. However, as *IRIS* began the scan off the solar disk and then progressed across the SST/CRISP FOV, only those data sampled between 08:10:00 UT and 08:20:00 UT are co-temporal and co-spatial to the SST/CRISP data set. Slit-jaw images (SJIs) were sampled by the 1400, 2796, and 2832 Å filters with cadences of 18.6 s, 18.6 s (with every fifth frame skipped to collect 2832 Å images), and 93 s, respectively. The spatial resolution of these data was ∼0.″33. Alignment of these data to the SST/CRISP, and hence the *SDO*/AIA, FOV, was completed by correlating the 2832 Å channel to wide-band Ca II 8542 Å images. The *IRIS* spectral data had an exposure time of ∼8 s and a spectral dispersion of approximately 0.026 Å for both the NUV and FUV windows.

2.1. Feature Identification

Candidate QSEBs were selected by locating small-scale (<2″), short-lived (1 < lifetime < 15 minute) regions of intense brightness (over 130% of the local background intensity) in the near wings (±1 Å) of the Hα line profile. This threshold is lower compared to the 150% threshold used by, for example, Vissers et al. (2013) and Nelson et al. (2015) and was selected due to the inherent lower line wing intensity enhancements identified co-spatial to QSEBs by Rouppe van der Voort et al. (2016). Next, we specified that the proportional increase in intensity from the background decreased farther out in the wings (±2 Å) in order to differentiate QSEBs from magnetic concentrations (MCs or "pseudo-EBs"; see Rutten et al. 2013), which are known to increase the continuum intensity. Once the candidate QSEBs had been detected, the Hα line core images were examined in order to remove features that corresponded to Hα micro-flares (features with obvious emission in the Hα line core). Finally, apparent explosive behavior (rapid morphological evolutions widely associated with EBs; Nelson et al. 2015; Vissers et al. 2015) was required, allowing us to confidently remove any remaining MCs. Overall, 21 QSEBs were located in this data set for further study.

Three of the QSEBs selected for analysis here are presented in Figure 2 for reference. The frames in the top row feature Hα blue wing (−1 Å), line core, Ca II 8542 Å blue wing (−1 Å), and Ca II 8542 Å line core images co-spatial and co-temporal to individual QSEBs. A long, thin brightening reminiscent of the events studied by Rouppe van der Voort et al. (2016) can be observed in the Hα line wing for each example; however, no unambiguous increase in intensity can be observed in any other panel of these plots. Slight Ca II 8542 Å wing enhancements similar to one case presented by Rouppe van der Voort et al. (2016) were

evident in two QSEBs from our sample; however, inspection of the imaging data revealed blurred patches, dissimilar to the compact Hα features in both time and space, implying that these co-spatial brightenings may not be linked to the QSEBs themselves. The red crosses and white boxes in the top left panels of each column indicate the pixel and set of pixels used to construct QSEB (solid line) and time-averaged quiet-Sun reference (dashed line) profiles, respectively. These profiles are plotted in the bottom panels of Figure 2, where red crosses indicate the wavelength positions plotted in the upper row. Obvious increases in intensity are evident in the wings of the Hα line profile (peaking at approximately ± 1 Å) for each of these events, confirming their QSEB-like nature. The event plotted in the right column is the feature sampled by the *IRIS* slit during its lifetime.

3. Results

3.1. Properties of QSEBs Derived from Imaging Data

We begin our analysis by acquiring measurements of the lengths, widths, and lifetimes of the 21 QSEB events studied in this article using CRISPEX. These measurements allow QSEBs to be compared with the EBs discussed in the literature (specifically by Nelson et al. 2015, who used a data set with an identical spatial resolution, thereby obtaining exactly comparable results) and to reaffirm the properties of QSEBs reported by Rouppe van der Voort et al. (2016). In the top panel of Figure 3 we plot the lengths and widths of the sample of QSEBs measured here (diamonds) and the AR EBs discussed by Nelson et al. (2015; crosses). It is immediately evident that the QSEBs are, in general, smaller than their AR counterparts. The means of the lengths and widths of these QSEBs were found to be $0\farcs63$ ($\sigma = 0\farcs17$) and $0\farcs35$ ($\sigma = 0\farcs08$), respectively. In the bottom frame of Figure 3, we plot the length against the lifetime of these QSEB features and the EBs studied by Nelson et al. (2015). The mean lifetime of these QSEBs is approximately 120 s ($\sigma = 60$ s), around 1 minute higher than the value reported by Rouppe van der Voort et al. (2016). As the minimum possible lifetime of events in this sample was 53 s, it is likely that this difference is due to the relatively low cadence of the data analyzed here. Indeed, several events in our sample were observed to live for around 4 minutes, with seemingly repetitive parabolic "flaming" (see Figure 4) that occurred over the course of one or two frames. For consistency, we did not classify each individual flame as a separate event, thereby increasing the mean. Recalculating the mean to account for repetition within the sample lowers the average lifetime of these QSEBs to 106 s ($\sigma = 47$ s).

Of the 21 events analyzed here, 3 were observed to display such impulsive repetitive behavior over short timescales during their lifetimes. This behavior was not apparent in the majority of features studied by Rouppe van der Voort et al. (2016). In Figure 4, we plot the evolution of the left event presented in Figure 2 at 53 s intervals for three positions within the Hα line profile, namely -1 Å, the line core, and $+1$ Å. In the second column, a QSEB is easily observed that then reduces in intensity and length in the third column before appearing to extend once again in the fourth column. Through a close inspection of the imaging data during this time period, it is clear that the apparent fading and contraction of the QSEB are not due to a reduction in seeing quality but are instead a real change in the morphology of the event through time. In addition to such impulsive recurrence, we also found one location where at least three seemingly independent QSEBs occurred over the course of 15 minutes. Such recurrence, shown for AR EBs (see, for example: Qiu et al. 2000; Nelson et al. 2015), is thought, in line with the magnetic reconnection hypothesis, to be indicative of multiple releases of energy from the same spatial location, potentially due to flux build-up through time (see, for example, Reid et al. 2016).

SDO/AIA images co-spatial to these QSEBs were also analyzed. As with EBs identified in ARs (see, e.g., Vissers et al. 2013; Nelson et al. 2015), no signature of QSEBs was observed in the *SDO*/AIA 304 Å filter. In Figure 5, we plot expanded FOVs around the three QSEBs presented in Figure 2 for the Hα blue wing (-1 Å; left-hand panel), the *SDO*/AIA 1600 Å filter (central panel), and the *SDO*/AIA 1700 Å filter (right panel). The small-scale QSEBs (in the Hα data) are almost entirely covered by the red crosses, which indicate the pixels selected to construct the light curves in the bottom panels. No signature was observed co-spatial to any QSEBs in the *SDO*/AIA 1700 Å channel; however, the events plotted in the central and right columns of Figure 5 did appear to be linked to burst-like events in the *SDO*/AIA 1600 Å filter. The isolation of the UV intensity enhancement to the *SDO*/AIA 1600 Å data could be due to the increased emission of the TR C IV in that filter rather than enhancements in the continuum intensity, potentially indicating that increased Si IV emission would also be expected. The red boxes overlaid on the *SDO*/AIA images indicate the regions selected to construct light curves.

The Hα line wing light curves plotted in the top panels of the bottom row of Figure 5 depict the short-lived (of the order minutes) intensity increases that are indicative of the presence of the QSEBS. Both QSEBs displayed in the left (plotted through time in Figure 4) and right columns are repetitive through their lifetimes, with their individual peaks highlighted by the arrows. The dashed vertical lines indicate the frames plotted in the top row. The *SDO*/AIA 1600 Å light curves (middle row) plotted in the central and right columns display short-lived peaks in intensity co-temporal to the formation of the QSEBs, with the right column exhibiting the clearest example of this behavior. The intensity for the minutes surrounding the QSEB approaches 150% of the time-averaged local background intensity. These increases in *SDO*/AIA 1600 Å intensity, co-temporal to only a small fraction of these QSEBs, are comparable to the signatures identified co-spatial to EBs in ARs.

3.2. Links between QSEBs and IBs

As *IRIS* was conducting a raster from off the limb to the solar disk, only the six QSEB features that occurred between 08:10:00 UT and 08:20:00 UT were studied using data collected by the SJI. This sample included the features plotted in the central and right columns of Figures 2 and 5. In Figure 6 we plot the 1400 Å (second row), 2796 Å (third row), and 2832 Å (bottom row) responses to the QSEBs (plotted in the Hα blue wing in the top row). Of these events, two (the QSEBs displayed in the second and sixth columns, which correspond to the central and right events of Figure 5, respectively) were identified to form co-spatial to short-lived increases in intensity in the Si IV 1400 Å filter, which appeared analogous to IBs (see, for example, Peter et al. 2014; Vissers et al. 2015; Tian et al. 2016). None of the other four events were observed

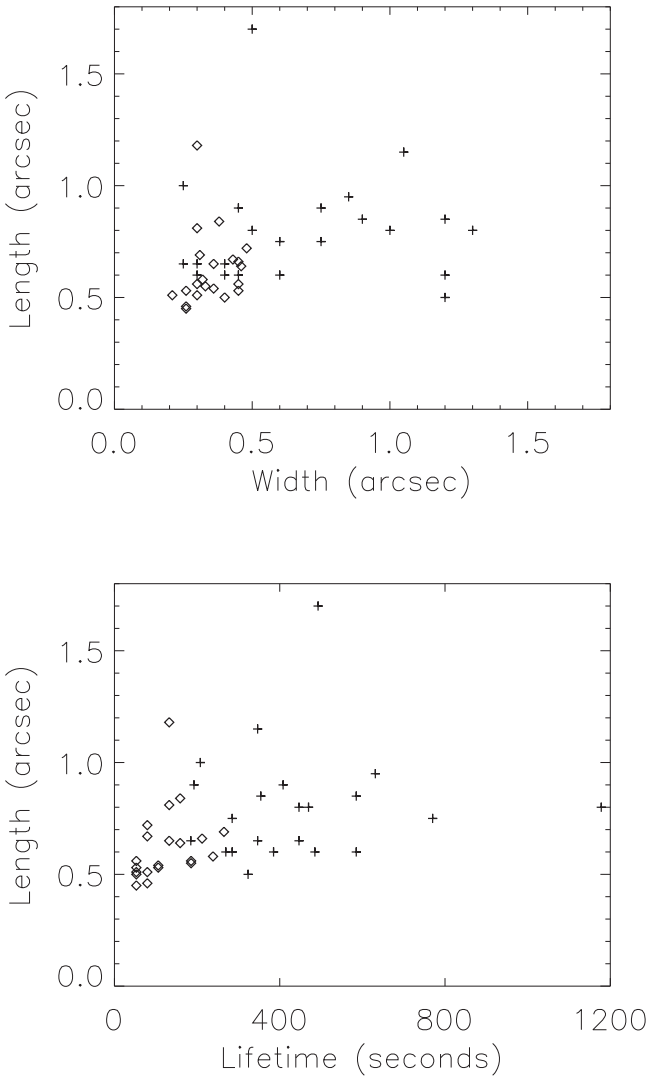

Figure 3. (Top row) Length against width plot for the QSEBs discussed in this article (diamonds) and EBs analyzed by Nelson et al. (2015; crosses). (Bottom row) Same as the top row except for the length against lifetime.

co-spatial to IBs, agreeing with the results of Rouppe van der Voort et al. (2016) that the majority of QSEBs display no TR signature. The two QSEBs that formed co-spatial to obvious *IRIS* signatures were neither particularly large, intense, or long-lived, appearing to be similar to the majority of QSEBs in this sample.

Interestingly, the feature in the right column of Figure 6 was also sampled by the *IRIS* slit during its lifetime, displaying an IB-like spectrum. In the top row of Figure 7, we plot the Si IV 1393 Å (left) and Si IV 1403 Å (right) spectral profiles sampled at the location of the IB (black line) and averaged over a quieter region close to this feature (red line). The bottom row shows the C II (left) and Mg II (right) spectra. Wavelength calibration was conducted following the method suggested by Tian et al. (2016). The Si IV 1393.755 Å window Doppler shift was estimated using the Ni II 1393.330 Å line (which was assumed to have zero Doppler shift). This shift was then also applied to the Si IV 1402.770 Å window. The C II spectral window was calibrated using the Ni II 1335.203 Å line (which, again, was assumed to have no Doppler shift). The accuracy of the detected shifts was confirmed by the similarity of the shifts in the Ni II 1393.330 Å and Ni II 1335.203 Å lines. The shift in the Mg II window was estimated using the neutral Mn I 2795.633 Å line.

The general shapes of the plotted spectral lines sampled at the location of the QSEB are similar to the IBs discussed in the literature (see, for example, Peter et al. 2014; Tian et al. 2016 for a variety of IB spectra), including wider and brighter Si IV profiles, increases in the Mg II and C II line wing intensities, and the absorption profiles of some chromospheric lines (for example, Ni II 1335.203 Å, Ni II 1393.330 Å, Fe II 1403.225 Å). The ratio between the intensities of the Si IV 1393 Å and Si IV 1403 Å lines at the location of the QSEB is ∼1.71, lower than that calculated for the reference profiles of ∼1.80 and the optically thin case of 2. In addition to this, some absorption is observed in the core of the Si IV 1393 line, consistent with the self-absorption discussed by Yan et al. (2015). These profiles provide the first evidence that certain QSEBs can occur co-spatial to IBs.

Quantitatively, the increases in intensity and line-width measured co-spatial to this QSEB are around an order of magnitude smaller than those previously reported around IBs (although it should be noted they are similar to some examples, including IB 5 discussed by Tian et al. 2016). This could be expected, however, given the reduced sizes and lower Hα line wing intensities of QSEBs in comparison to AR EBs (as well as the typically lower background intensities in the quiet-Sun). Interestingly, the Si IV line widths measured for this IB are smaller than those observed for most IBs in the literature. Potentially, this could be caused by the viewing angle as, if the bi-directional jets associated with the QSEB are predominantly vertical, only the limited line-of-sight components of such motions would be measured; however, this is currently only speculation.

In Figure 8, we plot spectral data for two additional IBs (with the same layout as applied in Figure 7) that occurred after the SST/CRISP instrument had stopped acquisition. Therefore, these events could not be linked to any QSEB. The Si IV spectra for both of the events plotted in Figure 8 displayed much larger line widths than the event plotted in Figure 7 that appears to be analogous to the features discussed by Tian et al. (2016). The ratios between the two Si IV lines are 1.83 and 1.47 for Examples 1 and 2, respectively, and again indicate a departure from the optically thin regime. It should be noted that the intensity enhancements in the Si IV line cores for Example 2 are twice those measured for the QSEB-linked IB and are therefore comparable to the intensities measured co-spatial to IBs in ARs by Tian et al. (2016).

The C II data for both IBs display broadened and enhanced line wings. The Mg II h&k peak intensities in Figure 8 are also slightly asymmetric, most likely due to velocity gradients in the atmosphere shifting the wavelength of maximum opacity to the red, causing increased emission in the blue peak. This effect has been described in detail in Carlsson & Stein (1997) and observed in the flare line profiles presented in Kuridze et al. (2015; for Hα) and Kerr et al. (2016; for Mg II). Both of the events plotted in Figure 8 also show evidence of self-absorption in the Si IV 1393 Å line, with Example 1 displaying clear self-absorption in the Si IV 1403 Å line as well. This self-absorption is also consistent with the scenario suggested by Yan et al. (2015), whereby the increased density within the feature causes absorption at the line core.

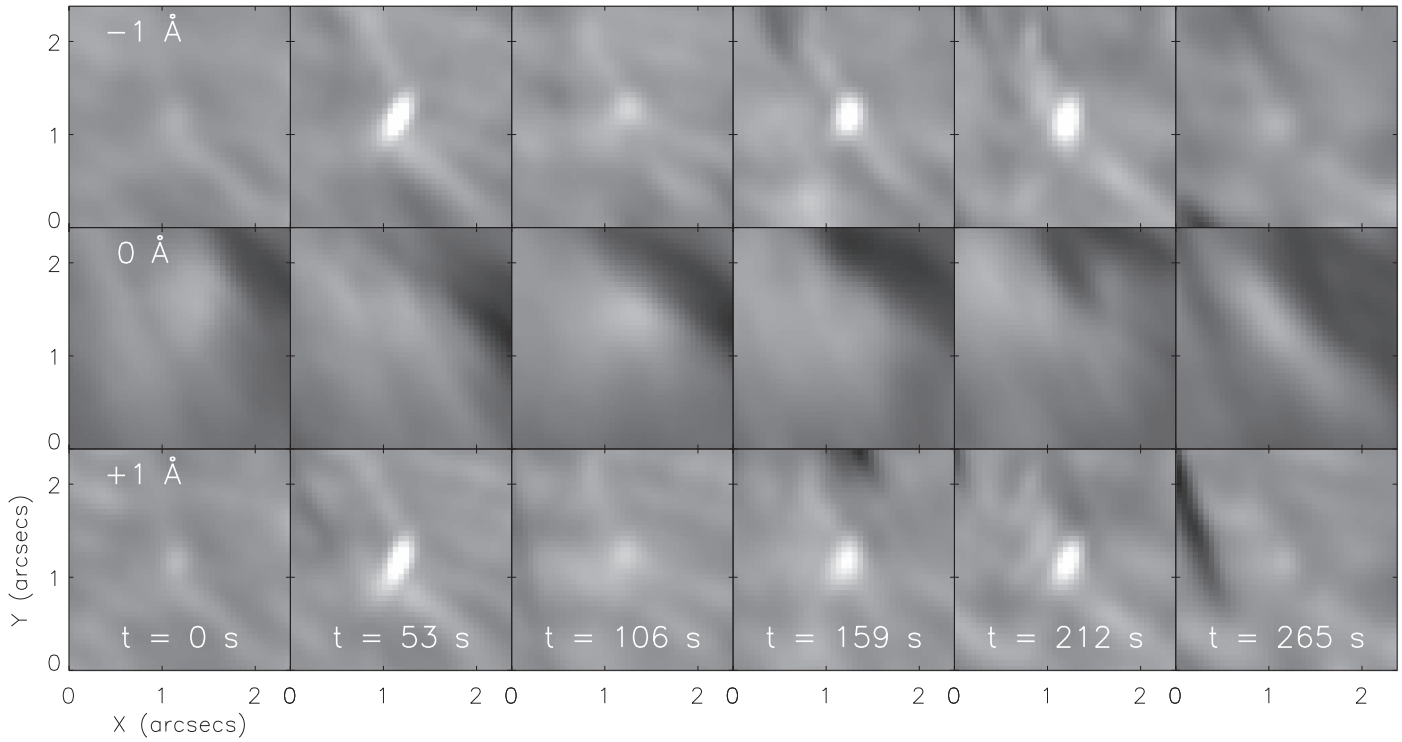

Figure 4. Evolution of a repetitive QSEB over the course of around four minutes in the blue wing (−1 Å; top row), line core (middle row), and red wing (+1 Å; bottom row) of the Hα line profile. A clear extension (second column) can be observed in the Hα line wings before its retraction (third column), and reemergence (fourth column). This behavior is similar to the evolution of certain EBs reported in the literature.

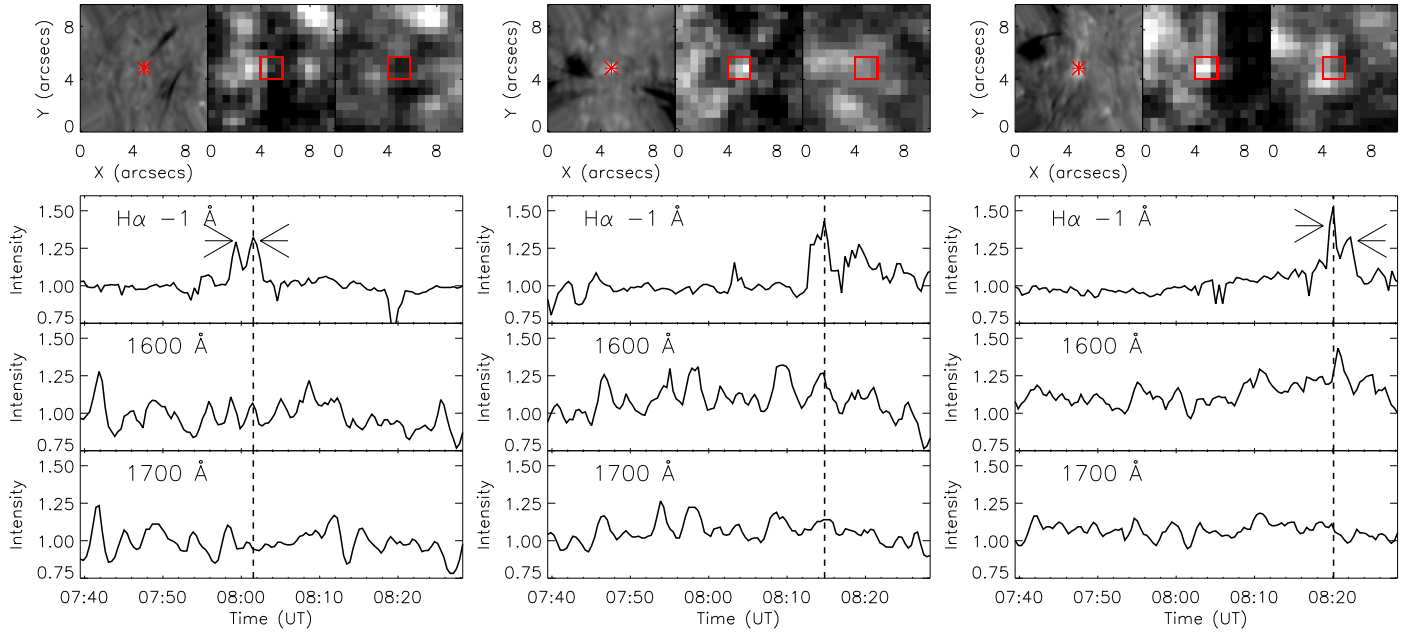

Figure 5. (Top row) Context images plotting the FOV surrounding the three QSEBs plotted in Figure 2. Included, respectively, from left to right for each column are: Hα red wing (−1 Å), *SDO*/AIA 1600 Å, and *SDO*/AIA 1700 Å images. The red crosses on the Hα wing images and the red boxes overlaid on the *SDO*/AIA channels indicate the pixel/regions used to construct light curves. (Bottom row) Light curves for each QSEB made for the Hα red wing (top panel), *SDO*/AIA 1600 Å channel (middle panel), and *SDO*/AIA 1700 Å filter (bottom panel). The dotted vertical lines indicate the time at which the QSEB reached peak intensity in the Hα line wings, which corresponds to the frames plotted in the top row. The arrows in the left and right columns highlight repetitive "flames" during the lifetimes of the QSEBs.

3.3. Hα and Ca II 8542 Å Line Synthesis

Finally, we investigate one-dimensional RADYN simulations (Carlsson & Stein 1992, 1995) created by perturbing three quiet solar-like atmospheres by depositing energy at a range of heights (building on the work recently presented by Reid et al. 2017). The motivation of this work is to attempt to explain the profiles displayed in Figure 2, where the Hα wing intensities are enhanced but no Ca II 8542 Å response is observed. Rouppe van der Voort

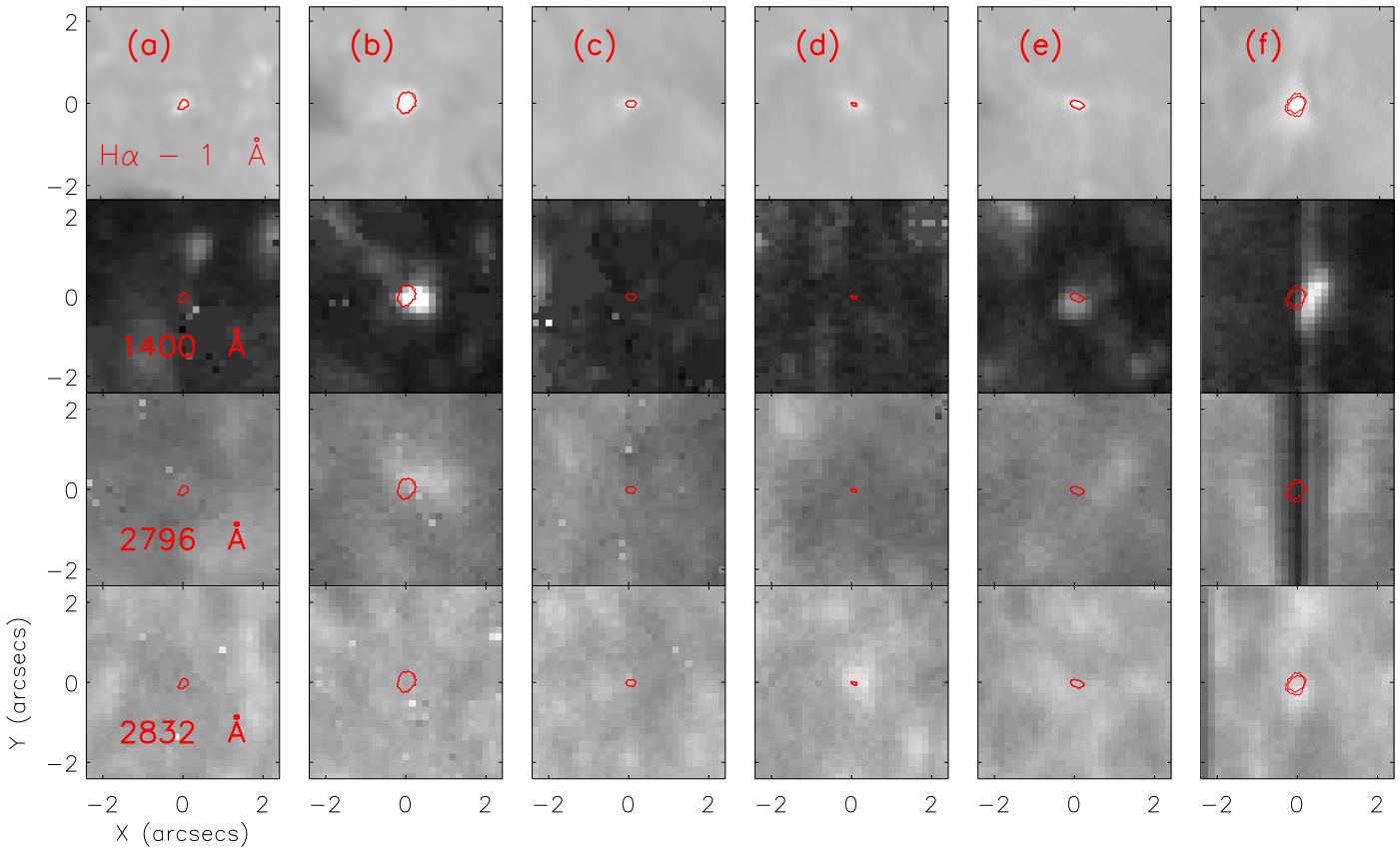

Figure 6. (Top row) The six QSEBs that occurred during the transit of the *IRIS* SJI across the SST/CRISP FOV. The features in the second and sixth columns were previously presented in Figures 2 and 5 (in the second and third columns of these figures, respectively). (Second row) The *IRIS* SJI 1400 Å response to these events, depicting the co-spatial formation of IBs (in the second and sixth columns). The co-spatial *IRIS* SJI 2796 Å (third row) and 2832 Å (bottom row) data are also included for completeness. The red contours indicate the pixels over 130% of the background intensity in the Hα line wings (i.e., the locations of the QSEBs).

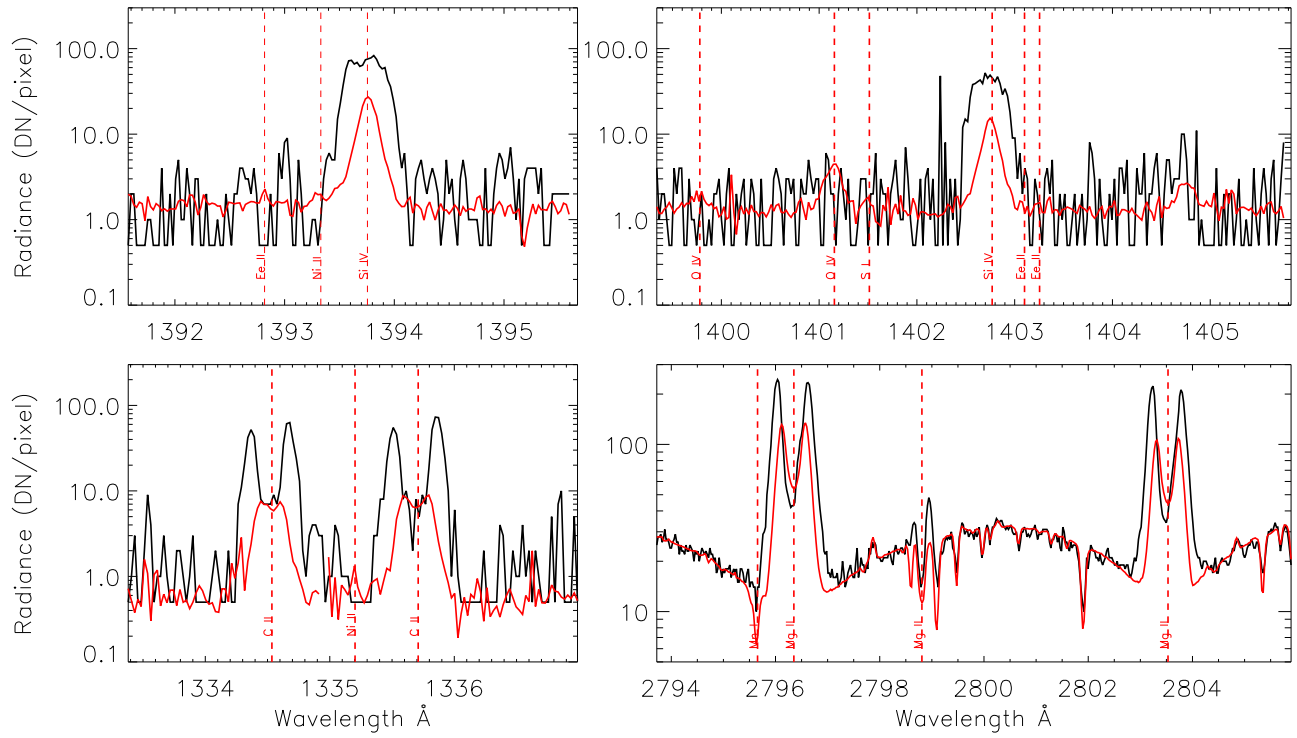

Figure 7. (Top row) The left and right columns, respectively, plot Si IV 1394 Å and Si IV 1403 Å spectral profiles for the IB pixel (black line) and an averaged reference profile (red line). (Bottom row) Spectral profiles for the C II and Mg II doublets sampled at the same locations as the top row. Note the logarithmic scaling of the *y*-axis. The vertical red dashed lines (and the corresponding labels) indicate the spectral locations of specific lines of interest to this analysis.

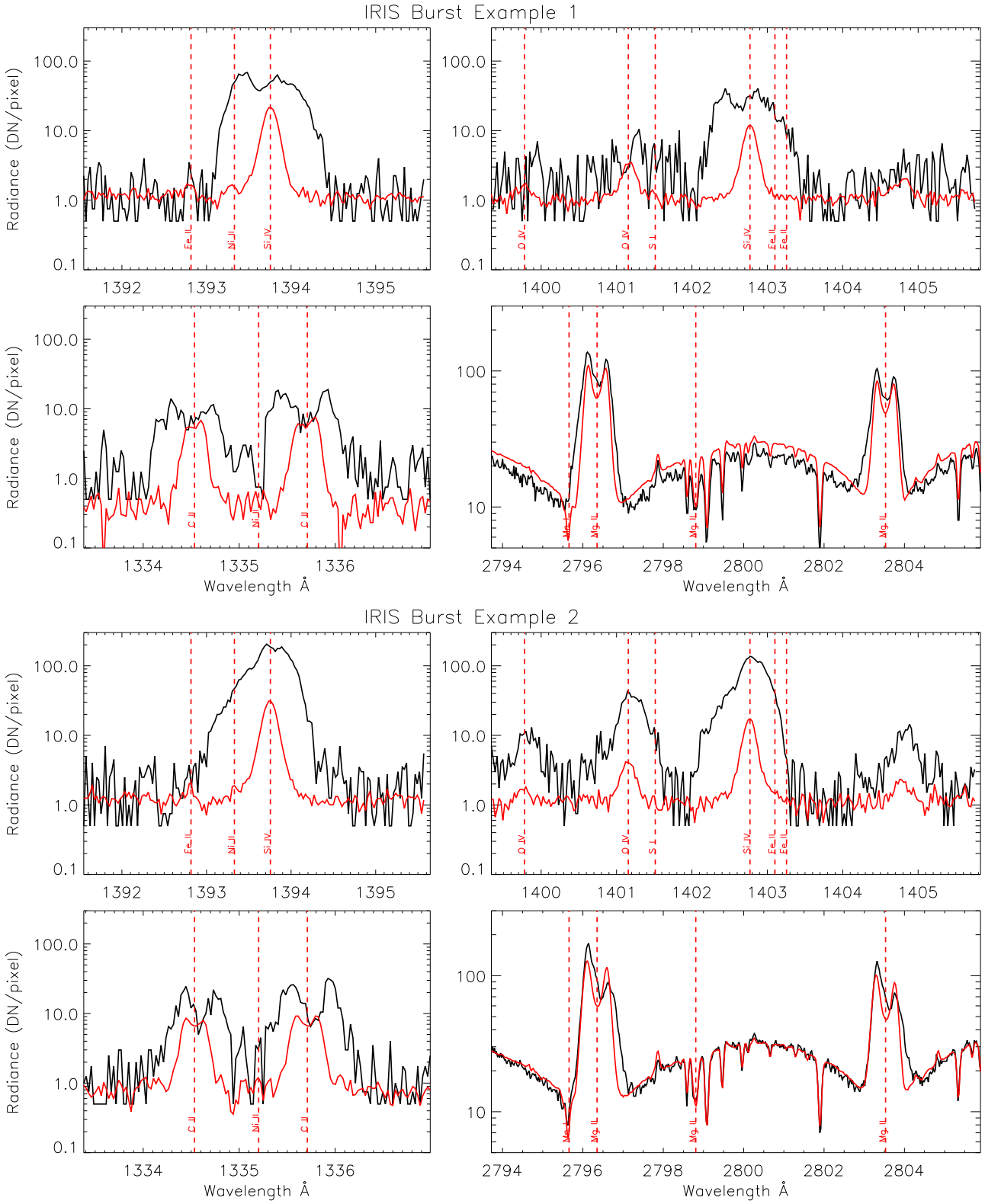

Figure 8. Same as Figure 7 but for two additional examples of *IRIS* burst-like events observed in these data.

et al. (2016) suggested that this observational signature is caused by the occurrence of the QSEB at heights that do not influence the Ca II 8542 Å line. Whether such layers exist still requires verification. We conducted a large range of simulations where either 100 erg cm^{-3} s^{-1}, 300 erg cm^{-3} s^{-1}, or 500 erg cm^{-3} s^{-1} of energy was inputted into a static atmospheric model at deposition layers (ranging from the photosphere to the chromosphere) that had heights of either 50 km or 200 km. We allowed the systems to stabilize for 9 s, before Hα and Ca II 8542 Å line profiles were constructed after 10 s of solar time using

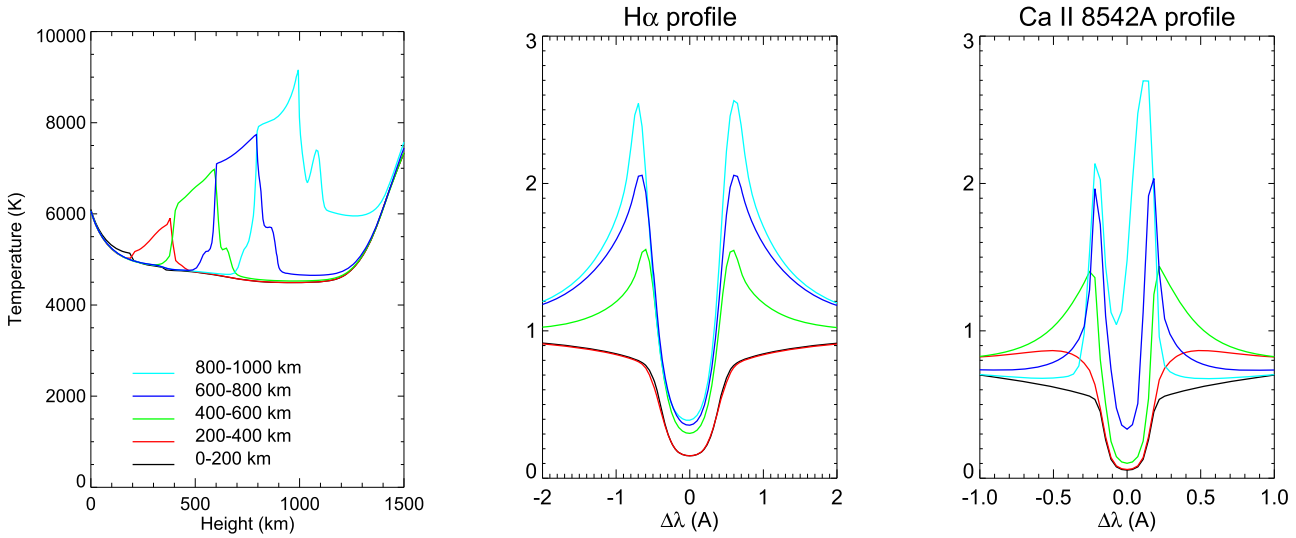

Figure 9. Five temperature profiles (left panel) corresponding to five 200 km high-energy deposition setups. The heights of each colored line are indicated in the legend. The Hα (center panel) and Ca II 8542 Å line profiles are synthesized for each one-dimensional atmosphere.

the MULTI package built into RADYN. Overall, more than 70 models were considered.

Before considering the results of these simulations, we briefly discuss the reasons for selecting the parameters introduced in the previous paragraph. First, we considered energy deposition layers of 50 and 200 km because smaller values would be below the spatial resolution of instruments such as the SST/CRISP, and larger layers would be well above the local scale height. Any energy deposition layers larger than 200 km would therefore not satisfy the condition that energy is deposited at a preferential location in the solar atmosphere, causing the observed spectral profiles of QSEBs. Second, the 500 erg cm^{-3} s^{-1} energy deposition rate was found to produce unrealistically high intensity enhancement in the Hα line profiles. Therefore, we do not consider any energy deposition rates higher than this. Energy deposition rates lower than 100 erg cm^{-3} s^{-1} did not provide the required Hα wing intensity increases and were also not considered. Finally, three different starting atmospheres (one quiet-Sun, as well as QS. SL.LT and QS.SL.HT from Allred et al. 2015) were studied, although the results obtained for each were comparable, so we only present results from the quiet-Sun atmosphere.

In the left panel of Figure 9, we plot examples of temperature profiles for five 200 km high-energy (300 erg cm^{-3} s^{-1}) deposition layer simulation runs, measured at $t = 10$ s. Each colored line in the left panel denotes a different energy deposition layer. These examples are representative of the entire suite of models that we studied. The center and right panels plot the respective Hα and Ca II 8542 Å synthesized line profiles. It is immediately evident that the higher that the energy is deposited in the atmosphere, the more emission the synthesized wings of both the Hα and Ca II 8542 Å lines display. In no case do the synthesized Hα wings form in emission when the Ca II 8542 Å wings do not. On the contrary, when the energy is deposited between 200–400 km, enhanced Ca II 8542 Å line wings are evident with no response from Hα. Qualitatively, these results do not change when one considers the shorter 50 km energy deposition bins. The line core intensities of both lines are also increased for higher-energy deposition layers, although this is probably due to the lack of three-dimensional effects (i.e., the lack of overlying canopy) in the simulations. Varying the energy deposition rate only changes the level of enhancement across both lines.

The strong connection between Hα line wing increases and Ca II 8542 Å line wing increases in these simulations comes from the modification of the contribution function of both lines due to the energy deposition. In the top panel of Figure 10, we plot the difference between the $t = 0$ s and $t = 10$ s contribution functions for the Hα line profile, for a representative 200 km high-energy deposition layer. The overlaid lines plot the synthesized line profile (green; arbitrary scaling) and the $\tau = 1$ height (red). The bright regions at a simulation height of 400 km and a Doppler shift of ± 20 km s^{-1} indicate the locations at which the enhanced emission in the Hα line wings (typical of EBs and QSEBs) occurs. The bottom panel plots the corresponding information for the Ca II 8542 Å line profile. This differenced contribution function also displays the bright regions (which are, perhaps, even more obvious than those in Hα) at Doppler shifts of around ± 20 km s^{-1}, which lead to increases in intensity in the Ca II 8542 Å line wings. Due to the change in the source function and opacity caused by the heating, the contribution of both the Hα and Ca II 8542 Å line wings increases at these heights, regardless of the quiet-Sun formation heights of these lines. Overall, these results do not appear to support the assertion that energy deposition, consistent with EBs and QSEBs, at specific heights in the solar atmosphere can lead to Hα wing emission without Ca II 8542 Å wing intensity enhancements. However, future work should aim to investigate this further, perhaps using different starting atmosphere models.

4. Discussion and Conclusions

QSEBs are an interesting newly discovered phenomenon, identified by increases in intensity in the Hα line wings similar to EBs (Ellerman 1917; Nelson et al. 2015; Vissers et al. 2015), but located in the quiet-Sun. These events are thought to highlight the occurrence of magnetic reconnection in the photosphere outside of ARs, perhaps similar to the modeling presented by Nelson et al. (2013) and Danilovic (2017). In this paper, we have not only corroborated the results of Rouppe van der Voort et al. (2016), but have also highlighted some new properties of these features, including repetition over both short

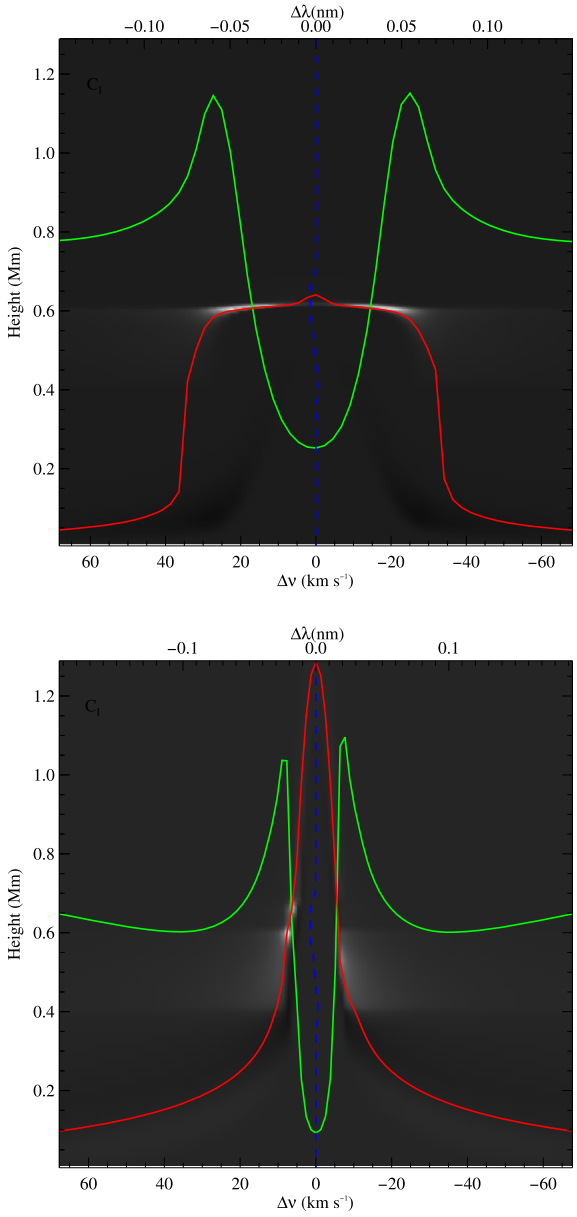

Figure 10. (Top panel) The difference between the contribution functions at $t = 0$ s and $t = 10$ s for the Hα line profile. The line profile at $t = 10$ s is overlaid in green. The red line indicates the $\tau = 1$ level. (Bottom panel) Same as the top panel but for the Ca II 8542 Å line profile.

and long timescales (in comparison to the lifetimes of the QSEBs), and shown the presence of an IB co-spatial to an individual QSEB (similar in nature to IB occurrence co-spatial to EBs; Tian et al. 2016), thereby also confirming the presence of IBs in the quiet-Sun. In the following paragraphs we shall present a brief overview of our results and discuss how they fit in with the current understanding of small-scale reconnection events.

Initially, 21 QSEBs were identified in Hα line scans collected at the solar limb by the SST/CRISP instrument. The basic properties of these events were comparable to those found by Rouppe van der Voort et al. (2016) with average lifetimes, lengths, and widths of approximately 120 s, 0.″63, and 0.″35, respectively. These values are at the lower end of the spectrum of properties previously derived for EBs in ARs, as is shown in Figure 3. Two features within this sample did appear co-spatial to limited (<120%) Ca II 8542 Å wing brightenings; however, as the bright regions in the Ca II 8542 Å line wings bore little resemblance to the clear, elongated QSEBs identified in Hα, it is likely that the Ca II 8542 Å heightened wing emission was not related to the QSEB. By studying a large range of RADYN simulated profiles, created by perturbed reference profiles by an input of energy, we were unable to reproduce line profiles that displayed enhanced Hα line wing emission and no Ca II 8542 Å response (see Figure 9).

Repetitive, impulsive flame-like behavior (shown to be common for EBs; see, e.g., Nelson et al. 2015; Vissers et al. 2015) was observed for three QSEB events in our sample. The evolution of one of these QSEBs is detailed in Figure 4 and the light curves constructed for that event and one additional example are plotted in the left and right columns of Figure 5, respectively, with the repetitive peaks indicated by the arrows. Such repetition was not widely observed either here or by Rouppe van der Voort et al. (2016), begging the question as to whether recurrence is common across the solar disk or whether it is only limited to certain regions with currently unknown similarities where, flux build-up perhaps occurs more readily (for example, at super-granular boundaries).

Two of these QSEBs formed co-spatial to burst events in the *SDO*/AIA 1600 Å UV and SJI 1400 Å data, with one of these events being sampled by the *IRIS* slit during its lifetime. The *IRIS* spectra displayed increased intensity in the Si IV 1393 Å and 1403 Å lines, as well as wing intensity increases in the C II and Mg II spectral windows (see Figure 7). These profiles were analogous to IBs discussed in the literature (Peter et al. 2014; Vissers et al. 2015; Tian et al. 2016). The Si IV line widths were smaller than the majority of IBs; however, this could be due to line-of-sight effects if the dominant motion of the QSEB is vertical away from the solar disk (i.e., perpendicular to the line of sight). Support for this assertion was found through analysis of several other IBs, which were identified in these data (presented in Figure 8). These IBs displayed larger Si IV line widths in addition to blueshifted Mg II profiles, potentially indicating velocities in the line of sight.

Overall, our results indicate that the majority of QSEBs are smaller and apparently weaker than their AR cousins, agreeing with the results of Rouppe van der Voort et al. (2016). However, the IBs co-spatial to two of these features indicate that that some (likely a small minority of) QSEBs could be linked to localized heating of plasma to TR temperatures, in a similar manner to energetic EBs in ARs. Future observational work should be carried out to discover how common such apparently energetic QSEBs are. It also remains to be seen whether the interesting Hα and Ca II 8542 Å signatures of QSEBs can be reproduced through further semi-empirical modeling.

IRIS is a NASA small explorer mission developed and operated by LMSAL with mission operations executed at the NASA Ames Research center and major contributions to downlink communications funded by ESA and the Norwegian Space Centre. The Swedish 1 m Solar Telescope is operated on the island of La Palma by the Institute for Solar Physics of Stockholm University in the Spanish Observatorio del Roque de los Muchachos of the Instituto de Astrofísica de Canaries. SDO/AIA data courtesy of NASA/SDO and the AIA science team. This work was inspired by discussion at the "Solar UV bursts—a new insight to magnetic reconnection" meeting at the International Space Science Institute (ISSI) in Bern. We would like to thank the anonymous referee for useful comments that

improved this work. C.J.N. and R.E. thank the Science and Technology Facilities Council (STFC) for the support received to conduct this research. R.E. acknowledges the support received by the CAS Presidents International Fellowship Initiative, grant No. 2016VMA045, and is also grateful to the Royal Society for their support. R.O. acknowledges support from MINECO and FEDER funds through grant AYA2014-54485-P. We also thank Luc Rouppe van der Voort for invaluable help with data reductions.

ORCID iDs

C. J. Nelson https://orcid.org/0000-0003-1400-8356
A. Reid https://orcid.org/0000-0002-7695-4834
R. Oliver https://orcid.org/0000-0003-4162-7240
M. Mathioudakis https://orcid.org/0000-0002-7725-6296
R. Erdélyi https://orcid.org/0000-0003-3439-4127

References

Allred, J. C., Kowalski, A. F., & Carlsson, M. 2015, ApJ, 809, 104
Archontis, V., & Hood, A. W. 2009, A&A, 508, 1469
Berlicki, A., & Heinzel, P. 2014, A&A, 567, A110
Carlsson, M., & Stein, R. F. 1992, ApJL, 397, L59
Carlsson, M., & Stein, R. F. 1995, ApJL, 440, L29
Carlsson, M., & Stein, R. F. 1997, ApJ, 481, 500
Danilovic, S. 2017, A&A, 601, A122
de la Cruz Rodríguez, J., Löfdahl, M. G., Sütterlin, P., Hillberg, T., & Rouppe van der Voort, L. 2015, A&A, 573, A40
De Pontieu, B., Title, A. M., Lemen, J. R., et al. 2014, SoPh, 289, 2733
Ellerman, F. 1917, ApJ, 46, 298
Fang, C., Tang, Y. H., Xu, Z., Ding, M. D., & Chen, P. F. 2006, ApJ, 643, 1325
Georgoulis, M. K., Rust, D. M., Bernasconi, P. N., & Schmieder, B. 2002, ApJ, 575, 506
Grubecka, M., Schmieder, B., Berlicki, A., et al. 2016, A&A, 593, A32
Judge, P. G. 2015, ApJ, 808, 116
Kerr, G. S., Fletcher, L., Russell, A. J. B., & Allred, J. C. 2016, ApJ, 827, 101
Kim, Y.-H., Yurchyshyn, V., Bong, S.-C., et al. 2015, ApJ, 810, 38
Kitai, R. 1983, SoPh, 87, 135
Kuridze, D., Mathioudakis, M., Simões, P. J. A., et al. 2015, ApJ, 813, 125
Lemen, J. R., Title, A. M., Akin, D. J., et al. 2012, SoPh, 275, 17
Libbrecht, T., Joshi, J., de la Cruz Rodríguez, J., Leenaarts, J., & Asensio Ramos, A. 2017, A&A, 598, A33
Lyot, B. 1944, AnAp, 7, 31
McMath, R. R., Mohler, O. C., & Dodson, H. W. 1960, PNAS, 46, 165
Nelson, C. J., Scullion, E. M., Doyle, J. G., Freij, N., & Erdélyi, R. 2015, ApJ, 798, 19
Nelson, C. J., Shelyag, S., Mathioudakis, M., et al. 2013, ApJ, 779, 125
Pariat, E., Aulanier, G., Schmieder, B., et al. 2004, ApJ, 614, 1099
Peter, H., Tian, H., Curdt, W., et al. 2014, Sci, 346, 1255726
Qiu, J., Ding, M. D., Wang, H., Denker, C., & Goode, P. R. 2000, ApJL, 544, L157
Reid, A., Mathioudakis, M., Doyle, J. G., et al. 2016, ApJ, 823, 110
Reid, A., Mathioudakis, M., Kowalski, A., Doyle, J. G., & Allred, J. C. 2017, ApJL, 835, L37
Reid, A., Mathioudakis, M., Scullion, E., et al. 2015, ApJ, 805, 64
Rouppe van der Voort, L. H. M., Rutten, R. J., & Vissers, G. J. M. 2016, A&A, 592, A100
Rutten, R. J. 2016, A&A, 590, A124
Rutten, R. J., Rouppe van der Voort, L. H. M., & Vissers, G. J. M. 2015, ApJ, 808, 133
Rutten, R. J., Vissers, G. J. M., Rouppe van der Voort, L. H. M., Sütterlin, P., & Vitas, N. 2013, JPhCS, 440, 012007
Scharmer, G. B. 2006, A&A, 447, 1111
Scharmer, G. B., Bjelksjo, K., Korhonen, T. K., Lindberg, B., & Petterson, B. 2003, Proc. SPIE, 4853, 341
Scharmer, G. B., Narayan, G., Hillberg, T., et al. 2008, ApJL, 689, L69
Severny, A. B. 1956, Obs, 76, 241
Socas-Navarro, H., Martínez Pillet, V., Elmore, D., et al. 2006, SoPh, 235, 75
Tian, H., Xu, Z., He, J., & Madsen, C. 2016, ApJ, 824, 96
van Noort, M., Rouppe van der Voort, L., & Löfdahl, M. G. 2005, SoPh, 228, 191
Vissers, G., & Rouppe van der Voort, L. 2012, ApJ, 750, 22
Vissers, G. J. M., Rouppe van der Voort, L. H. M., & Rutten, R. J. 2013, ApJ, 774, 32
Vissers, G. J. M., Rouppe van der Voort, L. H. M., Rutten, R. J., Carlsson, M., & De Pontieu, B. 2015, ApJ, 812, 11
Watanabe, H., Kitai, R., Okamoto, K., et al. 2008, ApJ, 684, 736
Watanabe, H., Vissers, G., Kitai, R., Rouppe van der Voort, L., & Rutten, R. J. 2011, ApJ, 736, 71
Yan, L., Peter, H., He, J., et al. 2015, ApJ, 811, 48
Yang, H., Chae, J., Lim, E.-K., et al. 2016, ApJ, 829, 100